Journal of Alloys and Compounds 480 (2009) 782–787

Contents lists available at ScienceDirect

Journal of Alloys and Compounds

journal homepage: www.elsevier.com/locate/jallcom

Microstructure evolution in laser solid forming of Ti–50 wt% Ni alloy

Xiaojing Xu, Xin Lin, Mocong Yang, Jing Chen, Weidong Huang*

State Key Laboratory of Solidification Processing, Northwestern Polytechnical University, Xi'an 710072, PR China

ARTICLE INFO

Article history:
Received 20 September 2008
Received in revised form 11 February 2009
Accepted 14 February 2009
Available online 28 February 2009

Keywords:
Metals and alloys
Rapid-solidification
Laser processing
Phase transitions

ABSTRACT

Ti–50 wt% Ni alloys were fabricated by laser solid forming (LSF) using pure Ti and Ni powders. Effects of laser process parameters (laser power and scanning speed) on the deposited microstructures were investigated. With increasing scanning velocity and decreasing laser power, as-deposited microstructure exhibited an evolution from primary TiNi dendrite to two-phase TiNi + B2 dendrite and finally to TiNi + Ti_2Ni anomalous eutectic, meantime, the characteristic size of the dendritic arms also decreased. The experimental results were further compared with the model of Trivedi, Magnin, Kurz (TMK model) of eutectic growth and Kurz, Giovanola, Trivedi (KGT model) of dendrite growth. The experimental results are in a reasonable agreement with KGT model.

1. Introduction

Near equiatomic Ti–Ni alloys have attracted considerable attentions as functional materials for industrial and medical applications in recent years due to their excellent physical and chemical properties such as remarkable shape memory effect (SME), pseudoelasticity (PE), high corrosion resistance and good biocompatibility [1]. Otsuka and Ren [2] has investigated most of the fundamental issues of the alloys, such as martensitic transformations, diffusional transformations in the equiatomic and near equiatomic Ti–Ni alloys. Fukuda et al. [3] revealed the electronic structures of the main phases, and analyzed the stability of martensitic phases and precipitates in Ti–Ni alloys. Furthermore, Nagarajan and Chattopadhyay [4] characterized the detailed microstructures of rapid-solidified near equiatomic TiNi alloys containing small amount of Si, and described the trend of the refinement of the microstructure. More recently, Yamamoto et al. [5] studied the martensitic transformation and microstructure of Ti-rich Ti–Ni as-atomized powders, and Motemani et al. [6] found that Ni_3Ti intermetallic compounds have a great influence on martensitic phase transformation temperature of Ni-rich NiTi alloy, and further, Nama et al. [7] revealed the shape memory characteristics and relationship between microstructure and mechanical properties of Ti–45Ni–5Cu alloy.

Accompanying with the investigations on the microstructure of Ti–Ni alloys, many manufacturing technologies for near equiatomic Ti–Ni alloys were also developed, such as vacuum plasma spraying (VPS) [8], vacuum arc remelting [9], hot isostatic pressing (HIP) [10], equal channel angular extrusion (ECAE) [11] and self-propagation high temperature synthesis (SHS) [12]. However, these processes generally presented high manufacturing costs. Recently, laser solid forming (LSF) [13–14], a novel near-net-shape manufacturing route for metals, has been used to fabricate complex 3D components directly using CAD model of an object without special tools. LSF is also termed as directed light fabrication (DLF) [15], laser engineered net shaping (LENS) [16] and direct metal deposition (DMD) [17]. The freedom of selectively cladding different elemental powders or premixed blends and the employment of multiple powder feeder systems make it convenient to control the as-deposited composition and optimize the microstructure and properties for TiNi alloy. In this paper, Ti–50 wt% Ni (Ti–45.3 at.% Ni) dense bulk samples were prepared by LSF, the effects of laser processing parameters on the formation characteristics and microstructure evolution of TiNi alloys were examined. In addition, due to the solidification microstructure of LSFed Ti–Ni binary system shows dendrite and eutectic growth, the model of Trivedi, Magnin, Kurz (TMK model) of eutectic growth and Kurz, Giovanola, Trivedi (KGT model) of dendrite growth were employed to explain microstructural evolution. Actually, KGT and TMK model have been utilized successfully to analyze the microstructure evolution in Ti-Rene88DT [18] and SS316L-Rene88DT [19] functionally graded materials.

2. Experimental procedure

Ti–50 wt% Ni alloys were laser deposited in an argon shielded glove box using a 5 kW continuous wave CO_2. The premixed powder was fed into the molten pool using pure argon gas through a lateral nozzle, which was mounted on an overhead carriage. The laser beam was directed into the glove box through a window on top of the glove box.

---

* Corresponding author.
E-mail address: huang@nwpu.edu.cn (W. Huang).

0925-8388/$ – see front matter © 2009 Elsevier B.V. All rights reserved.
doi:10.1016/j.jallcom.2009.02.056

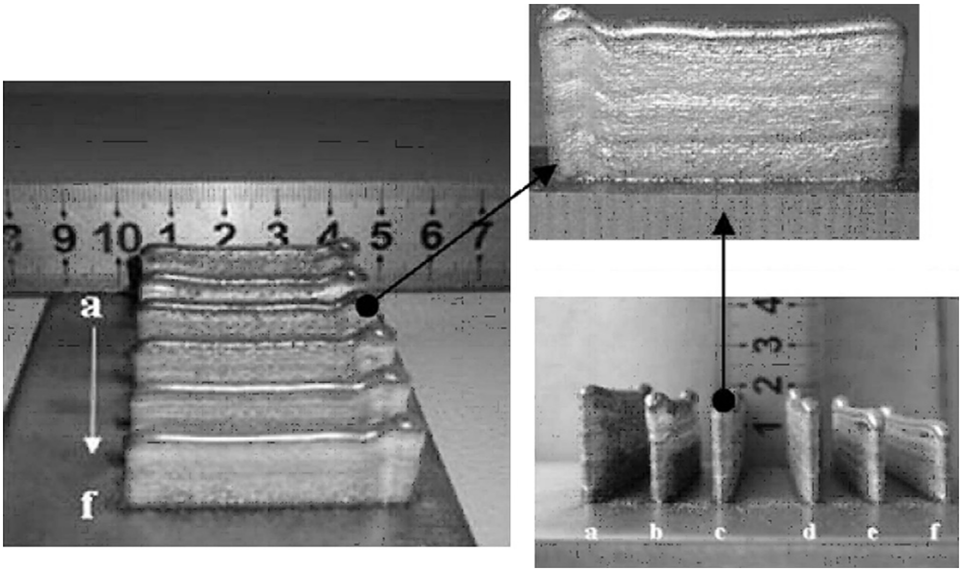

Fig. 1. Configuration of specimens under different laser processing parameters: (a) $P = 2$ kW, $v_s = 3$ mm/s; (b) $P = 2$ kW, $v_s = 5$ mm/s; (c) $P = 2$ kW, $v_s = 7$ mm/s; (d) $P = 3$ kW, $v_s = 6$ mm/s; (e) $P = 2.5$ kW, $v_s = 6$ mm/s; and (f) $P = 2$ kW, $v_s = 6$ mm/s.

A cold rolled Ti sheet with the dimensions of 140 mm × 60 mm × 4 mm was used as the substrate, which was sandblasted before LSF. The commercially pure Ti and Ni powders were used, which were dried over 24 h in a vacuum drying furnace and then premixed in a ball grinder before experiments. The average diameter of the powder was 150 μm.

The LSF processing parameters were as follows: the laser power (P) of 2–3 kW, the scanning speed (v_s) of 3–7 mm/s, the beam diameter (d) of 4 mm, the powder feeding rate of 10 g/min.

The as-deposited samples were sectioned perpendicular to the laser scanning direction and polished for metallographic characterization. The microstructure was characterized in detail using scanning electron microscopy (SEM) equipped with the facility of energy disperse X-ray spectroscopy (EDS).

3. Experimental results and discussion

The specimens free of macrocracks were obtained, as shown in Fig. 1. The XRD patterns of the as-deposited samples with different processing parameters are showed in Fig. 2. It can be seen that the as-deposited samples mainly consisted of Ti_2Ni and TiNi phases with a little B2 phase (ordered bcc β-Ti phase). Through comparing the relative diffraction peak strength among Ti_2Ni, TiNi and B2 phase in the same XRD pattern, it can deduced that, with increasing scanning velocity, the ratio of the volume fraction of Ti_2Ni to TiNi increased, and the volume fraction of B2 phase first increased then decreased. To have a more detailed investigation of phase transformation, the as-deposited microstructure were further studied by scanning electron microscopy. Figs. 3 and 4 show the SEM backscattered electron images of as-deposited microstructures with different processing parameters. For a given laser power of 2 kW, the as-deposited microstructure mainly consisted of TiNi dendrites in a Ti_2Ni matrix under low scanning velocity of 3 mm/s as shown in Fig. 3a, the microstructure changed to a two-phase TiNi(white phase) + B2(dark gray phase) dendrite in a Ti_2Ni matrix (Fig. 3b and c) with increasing the scanning velocity. Lin et al. [18] had found that there are some discrete NiCr-rich β-Ti particles (B2) close proximity to the dendrite arms of TiNi when the composition is above Ti–23Ni–4.8Co–7.2Cr (at.%) during laser solid forming of a functionally graded Ti-Rene88DT alloy. A mixture of two-phase TiNi + B2 dendrite and TiNi + Ti_2Ni anomalous eutectic (Fig. 3d) were obtained with further increasing the scanning velocity, which consists of a discontinuous TiNi particle in a continuous matrix of Ti_2Ni. On comparing Fig. 3c with Fig. 4a and b, it can be found that the microstructure will also change from two-phase TiNi + B2 dendrite (Fig. 3c and Fig. 4a) to a mix of TiNi dendrite and B2 dendrite (Fig. 4b) with increasing laser power under high scanning velocity. There are still different opinions about the formation mechanism(s) of anomalous eutectic [20–22]. To better underline the structure evolution process, a schematic diagram showing the solidification processes and the forming mechanisms was shown in Fig. 5.

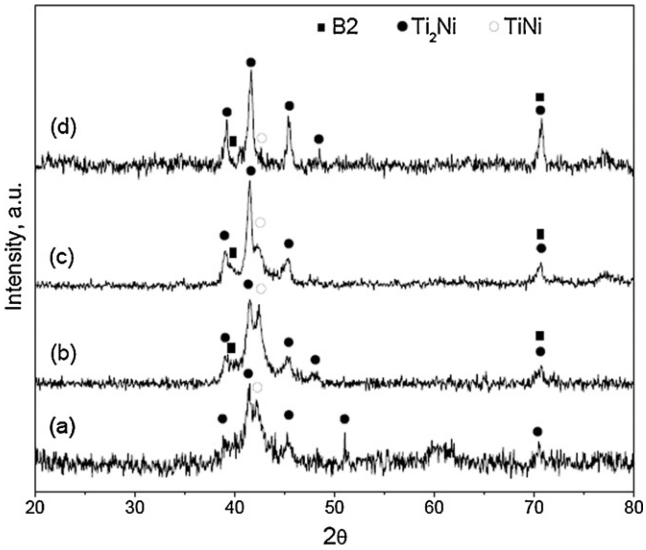

Fig. 2. The XRD patterns of the as-deposited samples with different laser processing parameter, (a) $P = 2$ kW, $v_s = 3$ mm/s; (b) $P = 2$ kW, $v_s = 5$ mm/s; (c) $P = 2.5$ kW, $v_s = 6$ mm/s; and (d) $P = 2$ kW, $v_s = 7$ mm/s.

For a given laser power and powder feed rate, the dendritic arm's size decreased with an increase in the scanning velocity (Fig. 2). For a given scanning velocity and powder feed rate, the dendritic arm's size increased with an increase in laser power on comparing Fig. 2c with Fig. 3.

3.1. Phase formation

Fig. 6a shows the equilibrium phase diagram of Ti–Ni alloy. Lin et al. [18] further calculated a solidification microstructure selection

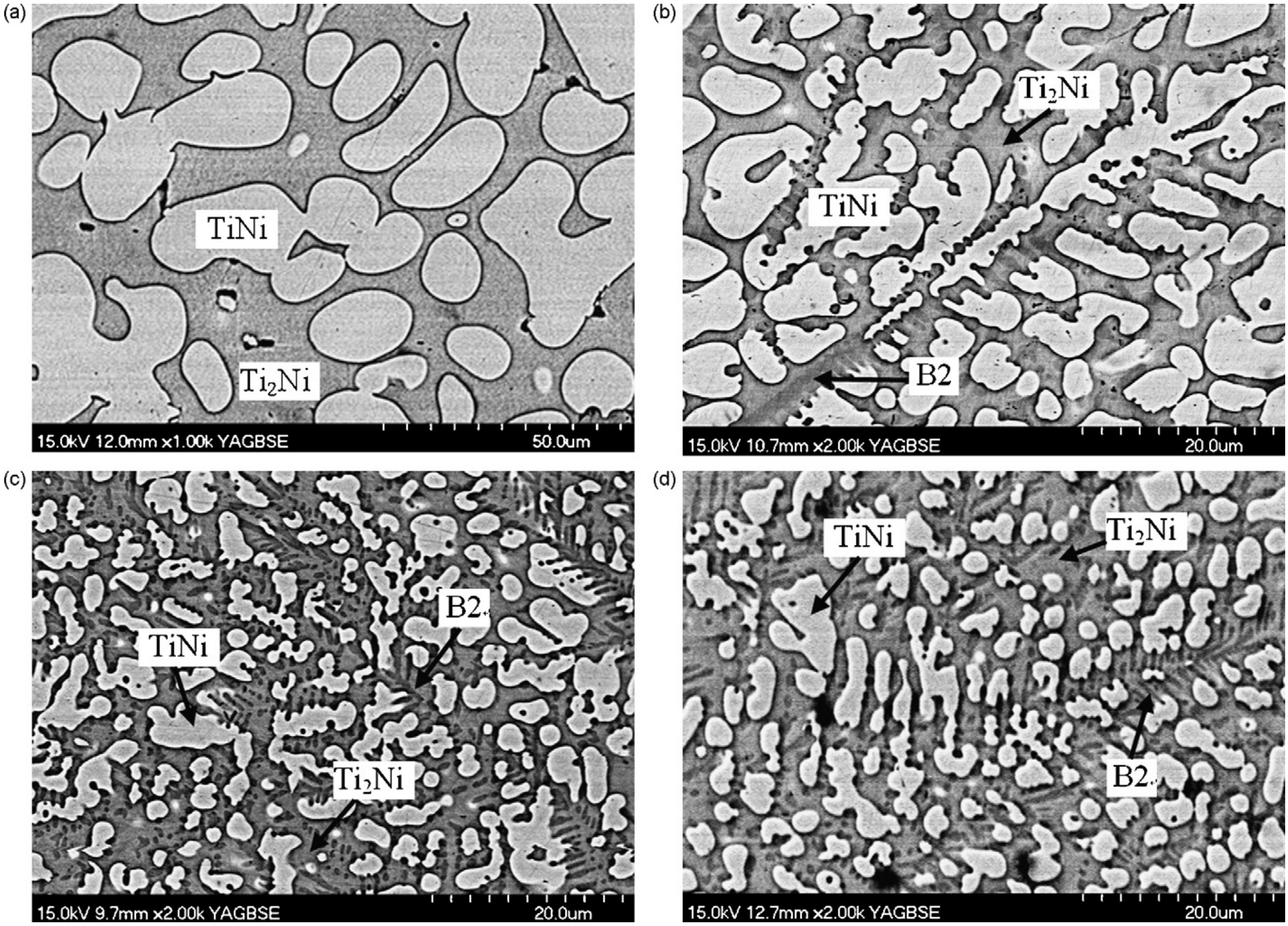

Fig. 3. SEM backscattered electron images of as-deposited microstructures obtained by the different laser processing parameter, $P = 2$ kW, (a) $v_s = 3$ mm/s, (b) $v_s = 5$ mm/s, (c) $v_s = 6$ mm/s, and (d) $v_s = 7$ mm/s.

map of Ti–Ni alloy system for the LSF process, as shown in Fig. 6b. It can be predicted from Lin's solidification microstructure selection map that the microstructure of Ti–50 wt% Ni alloys under LSF should be composed of TiNi dendrites. However, it is interesting to note that TiNi + B2 two-phase eutectic dendrite and TiNi + Ti_2Ni anomalous eutectics was observed under most of the processing parameter, as shown in Figs. 3b–d and 4a. It should be noted that two-phase eutectic dendrites usually appeared as the growth front of the anomalous eutectic grains [23]. In fact, Fig. 6a shows there should be a peritectic reaction of L + TiNi → Ti_2Ni, during the solidification of Ti–50 wt% Ni alloys. Perepezko and Boettinger [24] pointed out that there may be a transition from the peritectic phase diagram to a metastable eutectic phase diagram under non-equilibrium solidification condition. This is indicated by the contrasting signs between the stable liquidus and the metastable extension line of the liquidus of the secondary phase, and this transition will lead to a coupled growth. In rapid solidification, the phase region will be shifted due to the effect of the non-equilibrium interface and the capillary effect. Consequently, the metastable eutectic reaction will replace the conventional peritectic reaction. Such a condition is shown in Fig. 6a, where the intersection of the metastable liquidus of the Ti_2Ni and TiNi with contrary slopes is positioned. In fact, the liquidus of Ti_2Ni and TiNi will be further shifted to a lower temperature region as a result of a strong kinetic undercooling and the capillary effect during rapid solidification. Thus, an eutectic-like diffusional field would be established as a result of the rejection of Ni in front of the Ti_2Ni interface and Ti in front of the TiNi interface. Therefore, the thickness of the diffusion boundary layer is remarkably reduced and solute diffusion in front of solid–liquid interface satisfies the requirement of cooperative growth. This results in the evolution of Ti_2Ni + TiNi eutectic structures. Based on the measurement of the phase fraction of Ti_2Ni in the TiNi phase, the growth velocity threshold of coupled Ti_2Ni + TiNi eutectic growth was calculated through the TMK model [25]:

$$\lambda^2 v = \frac{\alpha^{\mathrm{L}}}{Q^{\mathrm{L}}} \tag{1}$$

$$\lambda \Delta T = m\alpha^{\mathrm{L}}\left[1 + \frac{p}{p + \lambda(\partial p/\partial \lambda)}\right] \tag{2}$$

λ is the lamellar spacing, and the definitions of the other terms are as follows, ΔT is the non-equilibrium eutectic undercooling;

$$\alpha^{\mathrm{L}} = 2\left\{\frac{\alpha_\alpha^{\mathrm{L}}}{fm_\alpha} + \frac{\alpha_\alpha^{\mathrm{L}}}{f(1-f)m_\beta}\right\} \tag{3}$$

$$Q^{\mathrm{L}} = \frac{1-k}{f(1-f)D}\left(p + \lambda\frac{\partial p}{\partial \lambda}\right) \tag{4}$$

$$p = \sum_{n=1}^{\infty}\left(\frac{1}{n\pi}\right)^3 [\sin(n\pi f)]^2 \frac{p_n}{\sqrt{1+p_n} - 1 + 2k} \tag{5}$$

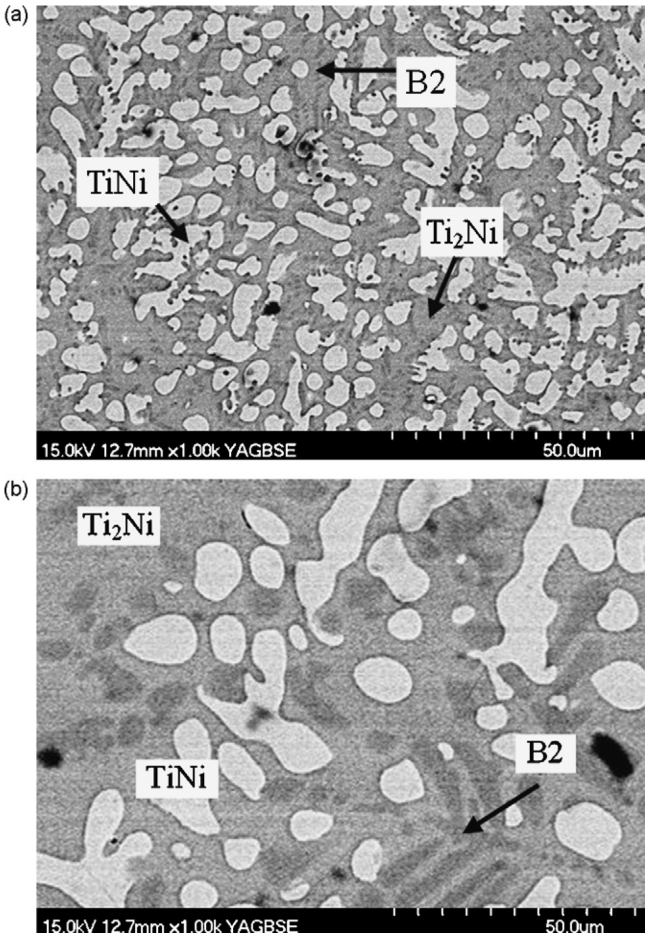

Fig. 4. SEM backscattered electron images of as-deposited microstructures obtained by the different laser processing parameter, $v_s = 6$ mm/s, (a) $P = 2.5$ kW and (b) $P = 3$ kW.

$$p+\lambda\left(\frac{\partial p}{\partial \lambda}\right)=\sum_{n=1}^{\infty}\left(\frac{1}{n\pi}\right)^{3}[\sin(n\pi f)]^{2}\frac{p_n}{\sqrt{1+p_n}-1+2k}\frac{p_n}{(1+p_n)^{1/2}} \tag{6}$$

where $P_n = 2n\pi/p$, $p = v\lambda/2D$, f is the volume fraction of the α-phase (TiNi) in the α + β eutectic (TiNi + Ti_2Ni eutectic), α_α^L and α_β^L are the capillarity constants of TiNi and Ti_2Ni, p is the solutal Peclet number. D is the liquid inter-diffusion coefficient, m is the liquidus slope, k is the solute distribution coefficient, v is the interface velocity.

According to Eqs. (1)–(6), the growth velocity threshold for coupled Ti_2Ni + TiNi eutectic growth was calculated out as 16 mm/s. It is believed that this velocity threshold was exceeded due to the deviation for thermo-physical parameters caused by rapid solidification when the scanning velocity is above 7 mm/s, and then Ti_2Ni + TiNi anomalous eutectic which represented by the simultaneous growth of Ti_2Ni dendrite and TiNi dendrite. It should be indicated that, for present work, when the solidification velocity is lower than the growth velocity threshold of coupled Ti_2Ni + TiNi eutectic growth, only TiNi + B2 two-phase eutectic dendrite was observed. It is possibly due to that the metastable TiNi + B2 eutectic growth temperature is higher than the metastable TiNi + Ti_2Ni eutectic growth temperature when the solidification velocity is not too high, which should resulted from the smaller equilibrium frozen temperature range of B2 (β-Ti) phase on comparison with that of Ti_2Ni phase based on the equilibrium phase diagram of Ti–Ni alloy (Fig. 6).

3.2. Effect of laser process parameters on the microstructure

TiNi dendrites act as the main phase as shown in Figs. 3 and 4. Hence, the following analysis is mainly based on the morphology of TiNi dendrites. However, it is difficult to recognize the primary or secondary arms of TiNi dendrites, so the characteristic dendritic size was then defined as follow: a group of parallel lines were set across the micrographs. The average number N of TiNi dendritic arms, through which each line passed, was counted; the characteristic dendritic size S is defined as $S = x/N$, x is the length of the valid measure-area. Actually, the characteristic size contains the informations of primary and secondary arms.

To clarify the influences of v_s and P on microstructure, the laser energy density (D_e) was defined as the following:

$$D_e = \frac{P}{dv_sM} \tag{7}$$

where d is the laser spot area that can be calculated by the laser beam diameter. M is the deposition amount of powders. D_e is a dimensionless parameter, which expresses the energy to melt the unit powder in unit time and area.

It can be seen from Fig. 7 that an increase in the laser energy density will cause the coarsening of dendrites. The characteristic size of S increases with D_e. In order to reveal the relationship between v and S, the KGT [26] model was used. According to KGT model, the variation of dendritic tip radius R with v can be described as follows:

$$v^2A + vB + C = 0 \tag{8}$$

where

$$A = \frac{\pi^2\Gamma}{p^2D^2} \tag{9}$$

$$B = \frac{mC_0(1-k)\xi_c}{D[1-(1-k)\mathrm{Iv}(p)]} \tag{10}$$

$$C = G$$

In which

$$\xi_c = 1 - \frac{2k}{\left[1+(2\pi/p)^2\right]^{1/2}-1+2k} \tag{11}$$

Γ is Gibbs–Thomson coefficient. C_0 is the initial liquid composition and $\mathrm{Iv}(p) = p\exp(p)E_1(p)$ is Ivantsov's solution. E_1 is the exponential integral function.

Furthermore, according to the Kurz and Fisher's analysis [23], the primary dendritic spacing can be expressed by a function of the dendritic tip radius as:

$$\lambda_1 = \sqrt{\frac{3\Delta TR}{G}} \tag{12}$$

where ΔT is the non-equilibrium solidification range, i.e. the difference between tip temperature and non-equilibrium solidus or eutectic temperature.

A number of studies on secondary dendrite arm spacing have been reported. It was found that there exists a definite scaling law between secondary dendrite arm spacing λ_2 and dendrite tip radius R. Huang and Glicksman [27] found a relationship of $\lambda_2/R = 3.0$ in pure undercooled succinonitrile. Somboonsuk et al. [28] got the result of $\lambda_2/R = 2.2$ in directionally solidified succinonitrile–4 wt%

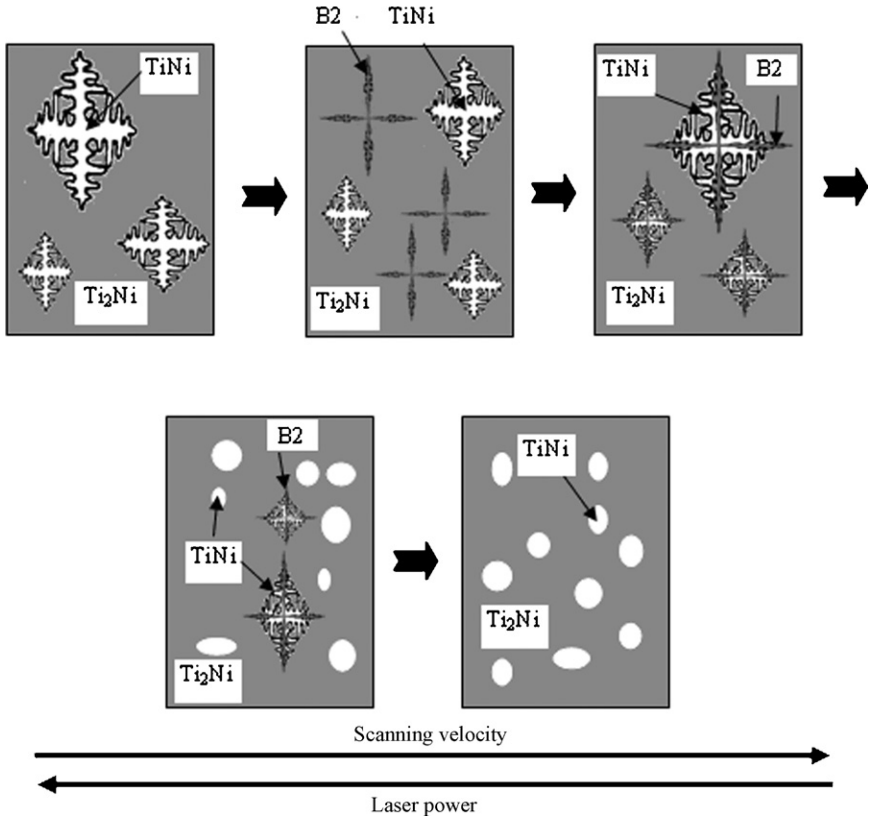

Fig. 5. Schematic diagram showing the solidification processes and the forming mechanisms of as-deposited microstructures which vary with the processing parameter.

acetone alloys. Trived and Somboonsuk [29] further examed Somboonsuk's result and obtained $\lambda_2/R = 2.0$. Therefore, it is reasonable to define λ_2 as follow:

$$\lambda_2 = 2R \tag{13}$$

The results of Eqs. (12) and (13) are presented in Fig. 8. It was found that the characteristic dendritic sizes S of TiNi dendrites lie between primary arm spacing λ_1 and secondary arm spacing λ_2. It should be noted that the characteristic dendritic size is effected by the solidification process to a large extent, and S is more close to predicted primary dendrite arm spacing at low velocity and predicted secondary dendrite arm spacing at high velocity. In fact, the microstructure presents typical TiNi dendrite growth at low scanning velocity, which will lead to relatively complete dendrite arms to enable S to represent the informations of primary dendrite; On the contrary, two-phase eutectic dendrite occurred with increasing the scanning velocity, a mixture of broken primary dendrite and discrete secondary dendrite make S more easily project secondary dendrite informations. As a whole, experimental results agree reasonably with the analysis of KGT model.

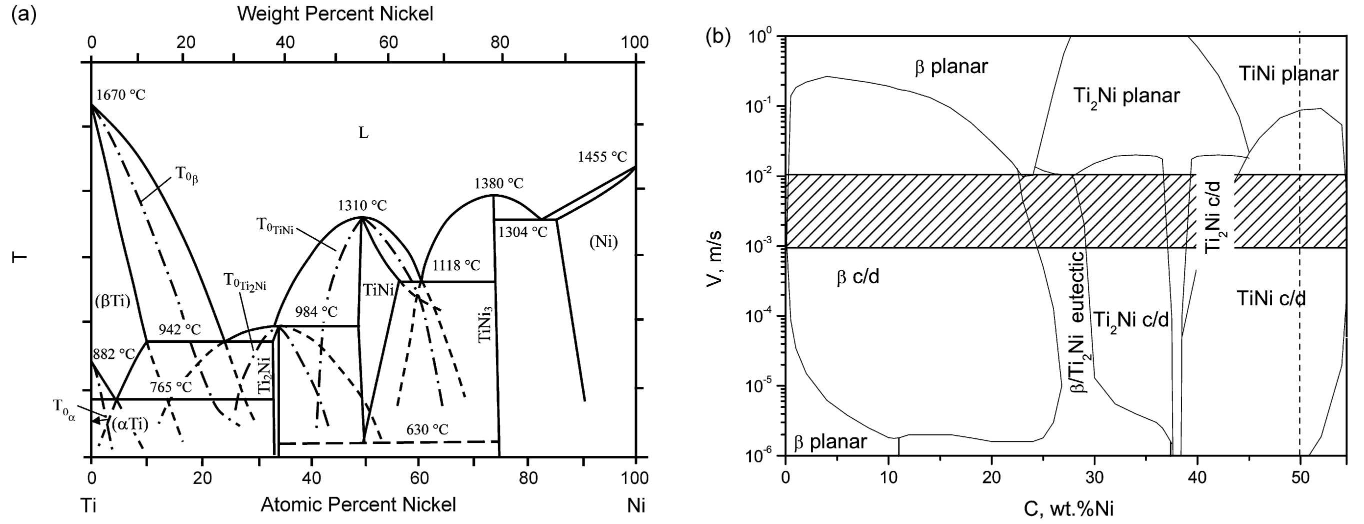

Fig. 6. Ti–Ni phase diagram and microstructure selection map: (a) a phase diagram of the Ti–Ni system after Ref. [13]; (b) a microstructure selection map for the Ti–Ni system, $G = 5 \times 10^5$ K/m [18].

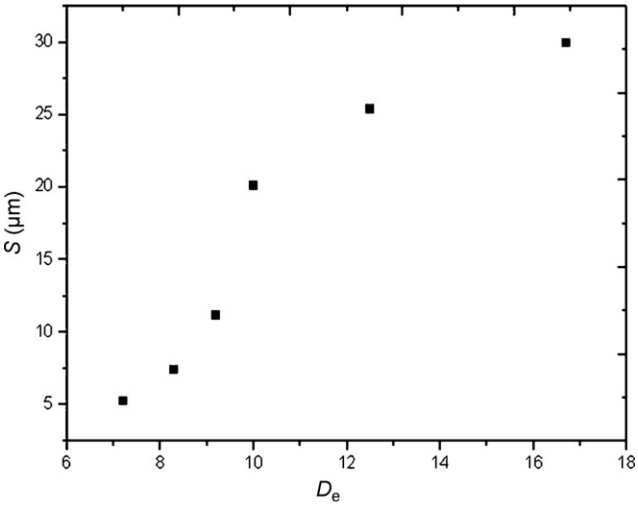

Fig. 7. Effect of D_e on the dendrite size ($G = 5 \times 10^5$ K/m).

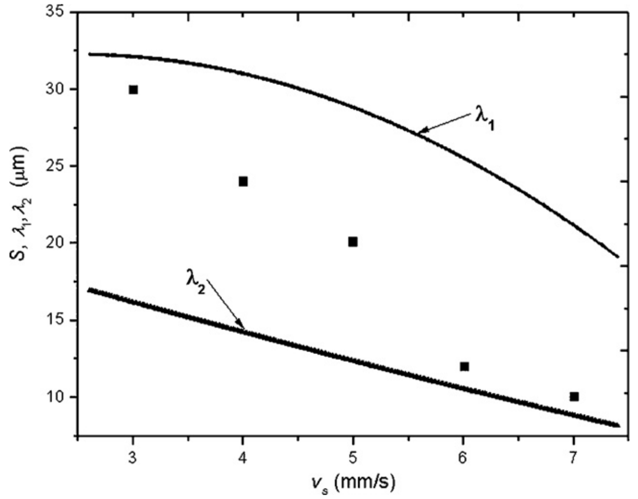

Fig. 8. Effect of v_s on the dendrite size ($G = 5 \times 10^5$ K/m).

4. Conclusions

1. Ti–50 wt% Ni alloy was deposited successfully by LSF. The microstructure consists of TiNi + B2 two-phase eutectic dendrite and TiNi + Ti_2Ni anomalous eutectics under most of the processing parameters.
2. The laser processing parameters had important effect on the microstructure. With increasing the scanning velocity and decreasing the laser power, the morphology of the microstructure exhibited an evolution from the primary TiNi dendrite to a two-phase TiNi + B2 eutectic dendrites and finally to TiNi + Ti_2Ni anomalous eutectic. It is believed that this velocity threshold of coupled Ti_2Ni + TiNi eutectic growth was exceeded due to the deviation for thermo-physical parameters caused by rapid solidification when the scanning velocity is above 7 mm/s. The formation of TiNi + B2 eutectic dendrites is possibly due to that the metastable TiNi + B2 eutectic growth temperature is higher than the metastable TiNi + Ti_2Ni eutectic growth temperature when the solidification velocity is not too high.
3. A characteristic size of the dendritic arms was defined. The characteristic size of the dendritic arms decreased with an increase in the scanning velocity and a decrease in the laser power. Regarding the scaling law between primary, secondary arm spacing and dendritic tip radius, the experimental results were further analyzed by KGT model. The characteristic dendritic size lies between the predicted primary and secondary arm spacings, which result from that primary TiNi dendrite growth at low scanning velocity and two-phase TiNi + B2 eutectic dendrite at high scanning velocity.

Acknowledgments

This work was supported by the program for New Century Excellent Talents in University of China (Grant No. NCET-06-0879), the National Natural Science Foundation of China (Grant No. 50331010), the National High Technology Research and Development Program (“863” Program) of China (Grant No. 2006AA03Z0449) and The National Basic Research Program (“973” Program) of China (Grant No. 2007CB613800).

References

[1] R. Lahoz, J.A. Puértolas, J. Alloys Compd. 381 (2004) 130–136.
[2] K. Otsuka, X. Ren, Prog. Mater. Sci. 50 (2005) 516–518.
[3] T. Fukuda, T. Kakeshita, H. Houjoh, Mater. Sci. Eng. A 273–275 (1999) 166–169.
[4] R. Nagarajan, K. Chattopadhyay, Acta Metall. Mater. 42 (1994) 947–958.
[5] T. Yamamoto, H. Kato, Y. Murakami, H. Kimura, A. Inoue, Acta Mater. 56 (2008) 5927–5937.
[6] Y. Motemani, M. Nili-Ahmadabadi, M.J. Tan, M. Bornapour, Sh. Rayagan, J. Alloys Compd. 469 (2009) 164–168.
[7] T.-H. Nama, J.-H. Lee, J.-M. Nam, K.-W. Kim, G.-B. Cho, Y.-W. Kim, Mater. Sci. Eng. A 483/484 (2008) 460–463.
[8] H. Nakayama, M. Taya, Mater. Sci. Eng. A 459 (2007) 52–59.
[9] A.L. Liu, Z.Y. Gao, L. Gao, J. Alloys Compd. 437 (2007) 339–343.
[10] D.S. Li, Y.P. Zhang, G. Eggeler, X.P. Zhang, J. Alloys Compd. 470 (2009) L1–L5.
[11] X.H. Cheng, Z.H. Li, G.Q. Xiang, Mater. Des. 28 (2007) 2218–2223.
[12] C.L. Yeh, W.Y. Sung, J. Alloys Compd. 376 (2004) 79–88.
[13] L. Xue, M.-U. Islam, J. Laser Appl. 12 (2000) 160–165.
[14] Y.M. Li, H.O. Yang, X. Lin, W.D. Huang, J.G. Li, Y.H. Zhou, Mater. Sci. Eng. A 360 (2003) 18–25.
[15] P.G. Li, T.P. Yang, S. Li, Int. J. Mach. Tools Manuf. 45 (2005) 1288–1294.
[16] X. Wu, J. Mei, J. Mater. Process. Technol. 135 (2003) 266–270.
[17] J. Mazumder, Q. Huan, Proc. SPIE 5706 (2005) 38–60.
[18] X. Lin, T.M. Yue, H.O. Yang, W.D. Huang, Acta Mater. 54 (2006) 1901–1915.
[19] X. Lin, T.M. Yue, Mater. Sci. Eng. A 402 (2005) 294–306.
[20] B. Wei, D.M. Herlach, B. Feuerbacher, F. Sommer, Acta Metall. Mater. 41 (1993) 1801–1809.
[21] M.J. Li, K. Nagashio, T. Ishikawa, S. Yoda, K. Kuribayashi, Acta Mater. 53 (2005) 731–741.
[22] X. Lin, T.M. Yue, H.O. Yang, W.D. Huang, Metall. Mater. Trans. A 38A (2007) 127–137.
[23] W. Kurz, D.J. Fisher, Fundamentals of Solidification, 3rd ed., Trans Tech Publications, Aedermansdorf, Switzerland, 1992.
[24] J.H. Perepezko, W.J. Boettinger, Mater. Res. Soc. Symp. Proc. 19 (1983) 223–240.
[25] R. Trivedi, P. Magnin, W. Kurz, Acta Metall. 35 (1987) 971–980.
[26] W. Kurz, B. Giovanola, R. Trivedi, Acta Metall. 34 (1985) 823–830.
[27] S.C. Huang, M.C. Glicksman, Acta Metall. 29 (1981) 701–715.
[28] K. Somboonsuk, J.T. Mason, R. Trivedi, Metall. Trans. A 15 (1984) 967–975.
[29] R. Trived, K. Somboonsuk, Mater. Sci. Eng. 65 (1984) 65–74.